Research Paper

Inference of Bubble Size Distribution in Sediments Based on Sounding by Chirp Signals

Xiaohong YANG[(1), (2)], Guangying ZHENG[(1), (2), (3)*], Fangyong WANG[(1), (2), (3)],
Fangwei ZHU[(1), (2)], Linlang BAI[(1), (2), (3)]

[(1)] *Science and Technology on Sonar Laboratory*
Hangzhou, China

[(2)] *Hangzhou Applied Acoustics Research Institute*
Hangzhou, China

[(3)] *Hanjiang National Laboratory*
Wuhan, China

*Corresponding Author e-mail: 276454158@qq.com

A method is proposed to estimate the bubble void fraction and bubble size distribution in marine sediments based on measured sound speed and attenuation data in gas-bearing sediments. The new inversion approach employs an effective density fluid model, corrected for gas bubble pulsations, as the forward model and represents the unknown gas bubble size distribution using a finite sum of cubic *B*-splines. An in situ acoustic monitoring experiment was conducted at an intertidal site in the Yellow Sea to investigate gassy sediments and validate the method. The measured sound speed and attenuation show significant fluctuations due to bubble resonance, with resonance peaks shifting to higher frequencies as water depth and hydrostatic pressure increase. This method simultaneously estimates the bubble size distribution from sound speed and attenuation data.

Keywords: gassy sediment; bubble size distribution; sound speed; attenuation; cubic *B*-splines.

1. Introduction

Characterizing the amount of gas within marine sediments is crucial, as gas bubbles can significantly affect acoustic reflection and penetration (RICHARDSON *et al.*, 1998; ANDERSON *et al.*, 1998; CHEN *et al.*, 2023). FLEISCHER *et al.* (2001) reported the global distribution of gas-bearing sediments and noted that these sediments are predominantly found in the Northern Hemisphere, particularly in shallow areas near Europe and the United States. In China, there is also a noticeable presence of shallow gas near the seabed in the South China Sea, East China Sea, and Yellow Sea. Generally, sediments containing gas bubbles exhibit pronounced sensitivity to acoustic waves, characterized by high dispersion and attenuation (LEIGHTON, 2007; YARINA *et al.*, 2023; ZHANG *et al.*, 2023). These acoustic properties of marine sediments are valuable for assessing the ecological status of the seabed. Consequently, the impact of bubbles on acoustic propagation is typically used to estimate the gas content and bubble size distribution within marine sediments (KARPOV *et al.*, 1996; LEIGHTON, ROBB, 2008). However, determining the bubble size distribution is generally more difficult than estimating the gas content of marine sediments.

In addressing the inverse problem of bubble size distribution (WILKENS, RICHARDSON 1998; BEST *et al.*, 2004; TÓTH *et al.*, 2015; EDRINGTON, CALLOWAY, 1984; SHANKAR *et al.*, 2005; 2006; FONSECA *et al.*, 2002), the forward model is typically based on Anderson and Hampton's (A&H) model (ANDERSON, HAMPTON, 1980a; 1980b), which remains the most widely used geoacoustic model for gas-bearing sedi-

ments. The A&H model is designed for linear bubble pulsation; however, its expression for complex sound speed includes both positive and negative signs, leading to ambiguities in the inverse problem concerning the bubble characterization (MANTOUKA et al., 2016).

The literature also highlights other effective inversion methods for estimating bubble size distributions in water and sediments. For example, COMMANDER and McDONALD (1991) and DOGAN et al. (2015) utilized a linear B-spline to approximate an unknown bubble size distribution, transforming the integral equation into a system of linear equations involving the coefficients of linear B-splines. Nonetheless, in this inversion method, attenuation is derived from the scattering and extinction cross-section a forward model that may not be suitable for accurately modeling gas-bearing sediments.

Accordingly, we propose an inversion method in this paper to estimate bubble size distributions. Our model integrates an acoustic model tailored for gas-bearing sediments with B-spline expansions. Additionally, both sound speed and attenuation are considered simultaneously in the inverse problem. This new inversion method utilizes an effective density fluid model (ZHENG et al., 2017), adapted to account for gas bubble pulsations as the forward model, and employs a finite sum of cubic B-splines to represent the unknown gas bubble size distribution. The inverse problem is reformulated as solving systems of equations that involve the coefficients of the cubic B-splines. This method has been validated using sound speed and attenuation data obtained from an in situ experiment conducted in the Yellow Sea.

2. Methodology

A corrected equivalent fluid density model, developed by ZHENG and HUANG (2016) and ZHENG et al. (2017), is utilized to predict sound speed and attenuation in gassy sediments. The model is expressed as

$$\nabla \left[K_{\text{eff}} \nabla \cdot \mathbf{u}_{\text{eff}} \right] = -\omega^2 \widetilde{\rho}_{\text{eff}} \mathbf{u}_{\text{eff}}, \quad (1)$$

where $\mathbf{u}_{\text{eff}}$ denotes the effective displacement. The effective modulus K_{eff} is expressed as follows:

$$K_{\text{eff}} = \left(\frac{(1-\beta)}{K_g} + \frac{\beta}{K_w} \right)^{-1}, \quad (2)$$

where K_g denotes the grain bulk modulus, K_w denotes the water bulk modulus, and β denotes the porosity. The corrected effective density is expressed as

$$\widetilde{\rho}_{\text{eff}} = \rho_{\text{eff}} + \int\limits_0^\infty \frac{4\pi\beta K_{\text{eff}} \rho_{\text{eff}} a f(a)}{\left\{ \rho_w \left[\omega_0^2(a) - \omega^2 + 2ib(a)\omega \right] \right\}} \, da, \quad (3)$$

$$\rho_{\text{eff}} = \frac{\left(\rho \widetilde{\rho} - \rho_w^2 \right)}{\left(\widetilde{\rho} + \rho - 2\rho_w \right)}, \quad (4)$$

$$\widetilde{\rho} = \frac{\alpha\rho_w}{\beta} - \frac{iF\eta}{\kappa\omega}, \quad (5)$$

$$\rho = \beta\rho_w + (1-\beta)\rho_g, \quad (6)$$

where ω denotes the angular frequency, η denotes the water viscosity, ρ_w denotes the pore fluid density, ρ denotes the sediment density, the permeability satisfies $\kappa = \frac{(d^2\beta^3)}{[180(1-\beta)^2]}$. The complex correction factor F is given by:

$$F(\varsigma) = \frac{\varsigma T(\varsigma)}{4\left(1 - \frac{2T(\varsigma)}{\varsigma}\right)},$$

$$T(\varsigma) = \frac{(ber'(\varsigma) + ibei'(\varsigma))}{(ber(\varsigma) + ibei(\varsigma))}, \quad (7)$$

$$\varsigma = a\left(\frac{\omega\rho_w}{\eta}\right)^{1/2},$$

where the pore size satisfies $a = \sqrt{\frac{8\alpha\kappa}{\beta}}$. The second item in Eq. (3) is the correction term for bubble pulsation, where $f(a)\,da$ is the number of bubbles per unit volume with radii between a and $a + da$. The parameter a is the bubble radius, and we use R to generally denote the bubble radius, ω_0 denotes the bubble resonance frequency:

$$\omega_0^2 = \left[\text{Re}\,\varphi - \frac{2\sigma}{(RP_{\text{in},0})} \right] \frac{P_{\text{in},0}}{\rho_w R^2}, \quad (8)$$

b denotes the damping term:

$$b = \frac{2\eta}{(\rho_w R^2)} + \frac{\omega^2 R}{(2c)} + \frac{\text{Im}\,(P_{\text{in},0}\varphi)}{(2\omega\rho_w R^2)}, \quad (9)$$

where φ is the polytropic exponent of the gas, expressed as

$$\varphi = \frac{3\gamma_g}{\left\{ 1 - 3(\gamma_g - 1)\,i\chi \left[\left(\frac{i}{\chi}\right)^{1/2} \coth\left(\frac{i}{\chi}\right)^{1/2} - 1 \right] \right\}}, \quad (10)$$

where c denotes the fluid phase velocity, σ denotes the surface tension, $P_{\text{in},0} = P_\infty + \frac{2\sigma}{R}$, P_∞ denotes the equilibrium pressure, $\chi = \frac{D}{\omega R^2}$, γ_g denotes the ratio of specific heat, and D denotes the thermal diffusivity of gas.

The complex velocity of gassy sediment is denoted as $c_1 = \sqrt{\frac{K_{\text{eff}}}{\widetilde{\rho}_{\text{eff}}}}$, and the phase velocity is

$$c_p = \frac{1}{\text{Re}\left(\frac{1}{c_1}\right)}. \quad (11)$$

The attenuation in decibels per meter is

$$\alpha^{(m)} = -\frac{20\omega\text{Im}\left(\frac{1}{c_1}\right)}{\ln 10}. \quad (12)$$

The absolute value of the effective density changes significantly due to bubble pulsation, leading to a decrease in the velocity of the porous medium. The imaginary part of the effective density accounts for an additional dissipation mechanism related to bubble pulsations. However, when the coefficient ratio defined in Eq. (13) is used to divide Eq. (1), Eq. (14) can be derived. Notably, the ratio is complex, with a modulus greater than 1 as long as the gas content is nonzero. As demonstrated in Eq. (14), bubble pulsation also modifies the sediment's effective modulus. In contrast, the sediment's effective density remains constant, resulting in a significant decrease in the sound speed of the medium:

$$\text{ratio} = \frac{\widetilde{\rho}_{\text{eff}}}{\rho_{\text{eff}}}$$

$$= 1 + \int\limits_0^\infty \frac{4\pi\beta K_{\text{eff}}af(a)}{\{\rho_w\left[\omega_0^2(a) - \omega^2 + 2ib(a)\omega\right]\}}\, \mathrm{d}a, \quad (13)$$

$$\nabla\left[\frac{K_{\text{eff}}}{\text{ratio}}\nabla \cdot \mathbf{u}_{\text{eff}}\right] = -\omega^2\rho_{\text{eff}}\mathbf{u}_{\text{eff}}. \quad (14)$$

Notably, in comparison to existing acoustic theories of gas-bearing sediments, the proposed model offers two significant advantages:

1) it incorporates the dispersion mechanism resulting from the relative motion between the pore water and the solid frame;

2) it provides independent expressions for sound speed and attenuation, in contrast to the A&H model, which enhances the applicability of the proposed model to inverse problems.

The reciprocal of the complex velocity can be derived from Eqs. (11) and (12):

$$\frac{1}{c_1} = \frac{1}{c_p} - i\frac{\alpha^{(m)}\ln 10}{20\omega}. \quad (15)$$

Combining Eq. (15) with $c_1 = \sqrt{\frac{K_{\text{eff}}}{\widetilde{\rho}_{\text{eff}}}}$, we obtain the following equation:

$$\frac{\widetilde{\rho}_{\text{eff}}}{K_{\text{eff}}} = \left(\frac{1}{c_p} - i\frac{\alpha^{(m)}\ln 10}{20\omega}\right)^2. \quad (16)$$

$\frac{\widetilde{\rho}_{\text{eff}}}{K_{\text{eff}}}$ can be derived from Eq.(3):

$$\frac{\widetilde{\rho}_{\text{eff}}}{K_{\text{eff}}} = \frac{\rho_{\text{eff}} + \int\limits_0^\infty \frac{4\pi\beta K_{\text{eff}}\rho_{\text{eff}}af(a)}{\{\rho_w[\omega_0^2(a) - \omega^2 + 2ib(a)\omega]\}}\, \mathrm{d}a}{K_{\text{eff}}}$$

$$= \frac{\rho_{\text{eff}}}{K_{\text{eff}}} + \int\limits_0^\infty \frac{4\pi\beta\rho_{\text{eff}}af(a)}{\{\rho_w[\omega_0^2(a) - \omega^2 + 2ib(a)\omega]\}}\, \mathrm{d}a. \quad (17)$$

A function $E(f)$ that varies with frequency is introduced to satisfy the relation in Eq. 17):

$$\int\limits_0^\infty \frac{4\pi\beta\rho_{\text{eff}}af(a)}{\{\rho_w\left[\omega_0^2(a) - \omega^2 + 2ib(a)\omega\right]\}}\, \mathrm{d}a$$

$$= \left(\frac{1}{c_p} - i\frac{\alpha^{(m)}\ln 10}{20\omega}\right)^2 - \frac{\rho_{\text{eff}}}{K_{\text{eff}}} = E(f). \quad (18)$$

The inverse of the bubble size distribution $f(a)$ is used to solve the first kind of Fredholm integral equation:

$$\int\limits_0^\infty \frac{4\pi\beta\rho_{\text{eff}}af(a)}{\{\rho_w\left[\omega_0^2(a) - \omega^2 + 2ib(a)\omega\right]\}}\, \mathrm{d}a = E(f). \quad (19)$$

To solve the integral Eq. (19), we use a finite sum of cubic B-splines to denote $f(a)$:

$$f(a) = \sum_{j=0}^{n+2} C_j\Omega_3\left(\frac{a - a_{j-1}}{h}\right), \qquad a_0 \le a \le a_1, \quad (20)$$

where $a_j = a_0 + jh$ ($j = 0, 1, ..., n$), $h = \frac{a_1 - a_0}{n}$, and C_j is the coefficient to be determined.

Substituting Eq. (20) into Eq. (19) yields a linear set of equations:

$$E(f_i) = \sum_{j=0}^{n+2} C_j K_{ij}, \quad (21)$$

where the elements of the matrix are

$$K_{ij} = \int\limits_0^\infty \frac{\Omega_3\left(\frac{a - a_{j-1}}{h}\right)4\pi\beta\rho_{\text{eff}}a}{\{\rho_w\left[\omega_0^2(a) - \omega^2 + 2ib(a)\omega\right]\}}\, \mathrm{d}a. \quad (22)$$

In matrix notation, Eq. (21) may be written as follows:

$$\begin{pmatrix} K_{11} & K_{12} & K_{13} & \cdots & K_{1N} \\ K_{21} & K_{22} & K_{23} & \cdots & K_{2N} \\ K_{31} & K_{32} & K_{33} & \cdots & K_{3N} \\ \vdots & \vdots & \vdots & & \vdots \\ K_{N1} & K_{N2} & K_{N3} & \cdots & K_{NN} \end{pmatrix}\begin{pmatrix} C_1 \\ C_2 \\ C_3 \\ \vdots \\ C_N \end{pmatrix} = \begin{pmatrix} E_1 \\ E_2 \\ E_3 \\ \vdots \\ E_N \end{pmatrix}. \quad (23)$$

The proposed inversion method has two primary advantages:

1) it transforms the nonlinear inverse problem by solving linear equation sets, thereby reducing computational demands;

2) it overcomes the ambiguities inherent in inversions based on the A&H model.

Consequently, this method is particularly well-suited for inverse problems that combine both sound speed and attenuation data, optimizing computational efficiency while accounting for both parameters.

To aid comprehension of the proposed method, we summarize it in the following steps:

1) select the control points for the cubic B-spline;

2) utilize Eq. (22) to calculate the matrix kernel K_{ij} based on frequency, measured physical parameters, and the selected control points;

3) apply Eq. (18) to calculate the function $E(f)$ based on the measured sound speed and attenuation coefficient;

4) calculate the coefficients of the cubic B-spline using the pseudo-inverse of matrix $\mathbf{K}$, and subsequently determine the bubble size distribution using Eq. (20).

Next, we present the simulation analysis of the inversion process for bubble size distribution utilizing the method developed in this section. A finite sum of cubic B-splines is employed to represent the unknown bubble size distribution, with the control points and their corresponding coefficients detailed in Table 1. Figure 1 illustrates the resulting bubble size distribution, while the physical parameters of the marine sediments are provided in Table 2. The sound speed and attenuation coefficient as functions of frequency are shown in Fig. 2. The results indicate that as the insonifying frequencies approach the resonance frequency of the bubble, the acoustic properties of gassy sediment exhibit significant dispersion, and the attenuation reaches its peak.

Table 1. Control points and their coefficients of cubit B-spline.

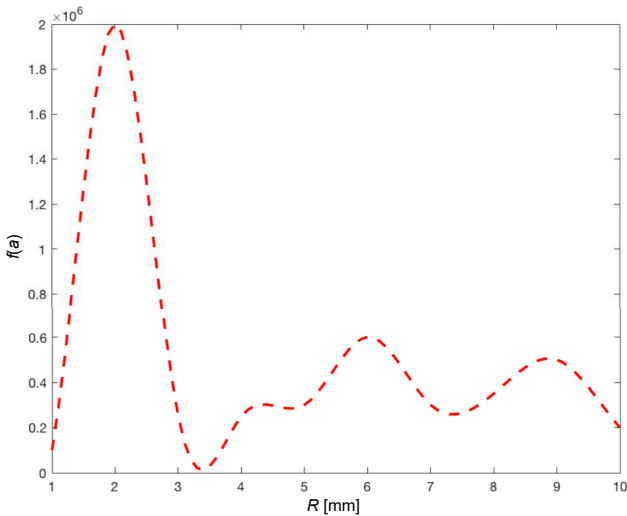| Control point [mm]	Coefficients ($\times 10^5$)
0	0
1	-6.8
2	33
3	-5.8
4	4.9
5	1.2
6	8.3
7	1.6
8	3.3
9	6.3
10	1.4
11	0

Fig. 1. Bubble size distribution.

Table 2. Input parameters.

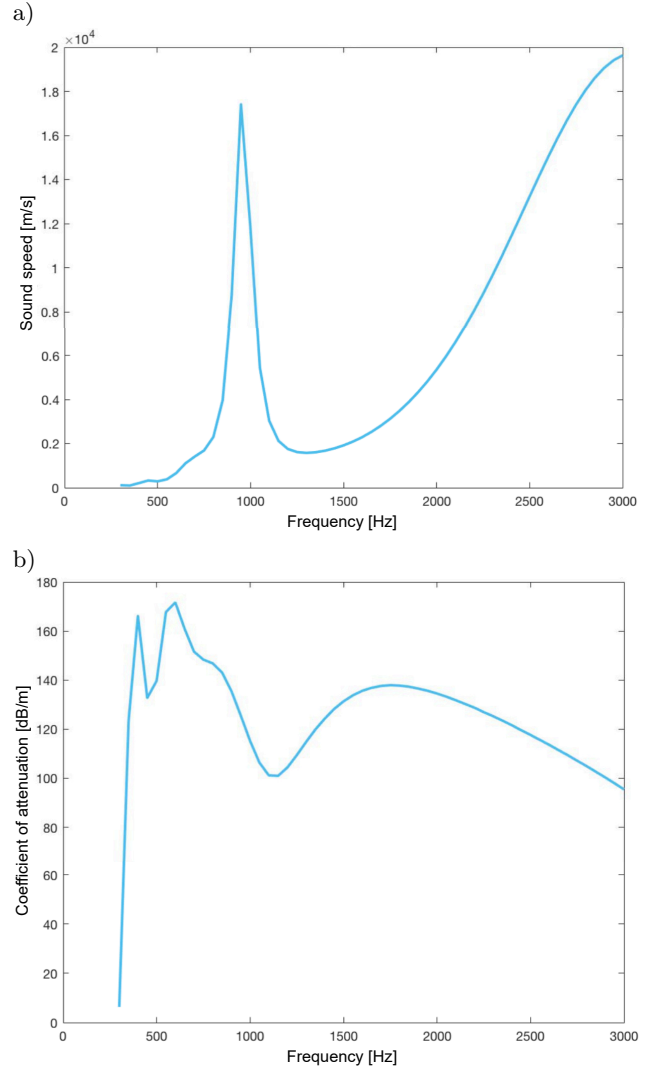|	Parameters	Values
Sediment parameters	Grain density	2465 kg/m^3
	Grain diameter	0.781 mm
	Fluid bulk modulus	2.193 Pa $\times 10^9$ Pa
	Grain bulk modulus	3.6 Pa $\times 10^{10}$ Pa
	Fluid viscosity	1.002 Pa$\cdot$s $\times 10^{-3}$ Pa$\cdot$s
	Porosity	0.37
	Fluid density	998.2 kg/m^3
	Structure factor	1.25
Gas parameters	Gas density	1.1691 kg/m^3
	Gas velocity	340 m/s
	Equilibrium pressure	1.01 Pa $\times 10^5$ Pa
	Thermal diffusivity	2.4 m^2/s $\times 10^{-5}$ m^2/s
	Surface tension	72.75 N/m $\times 10^3$ N/m
	Ratio of specific heat	1.4

a)

b)

Fig. 2. Variation in: a) sound speed; b) coefficient of attenuation with frequency.

In the simulation of bubble size distribution, this study evaluates the effects of random errors in sound

speed and attenuation data to analyze the robustness of the proposed inversion method in the presence of data errors. When controlling for attenuation data, the inversion results for bubble size distribution across varying sound speed error ranges are depicted in Fig. 3. Conversely, when controlling for sound speed data, the inversion results for bubble size distribution across different attenuation error ranges are presented in Fig. 4. Additionally, Fig. 5 illustrates the inversion results for bubble size distribution considering data errors in both sound speed and attenuation. In these figures, the solid line represents the inversion results derived from multiple random errors, whereas the dashed line indicates the true value of the selected bubble size distribution. From Figs. 3 and 4, we observe that satisfactory inversion results can be achieved with a sound speed error range of 1×10^{-3}, while a larger local error in bubble size distribution occurs with an error range of 2×10^{-3}. Similarly, good inversion results can be at-
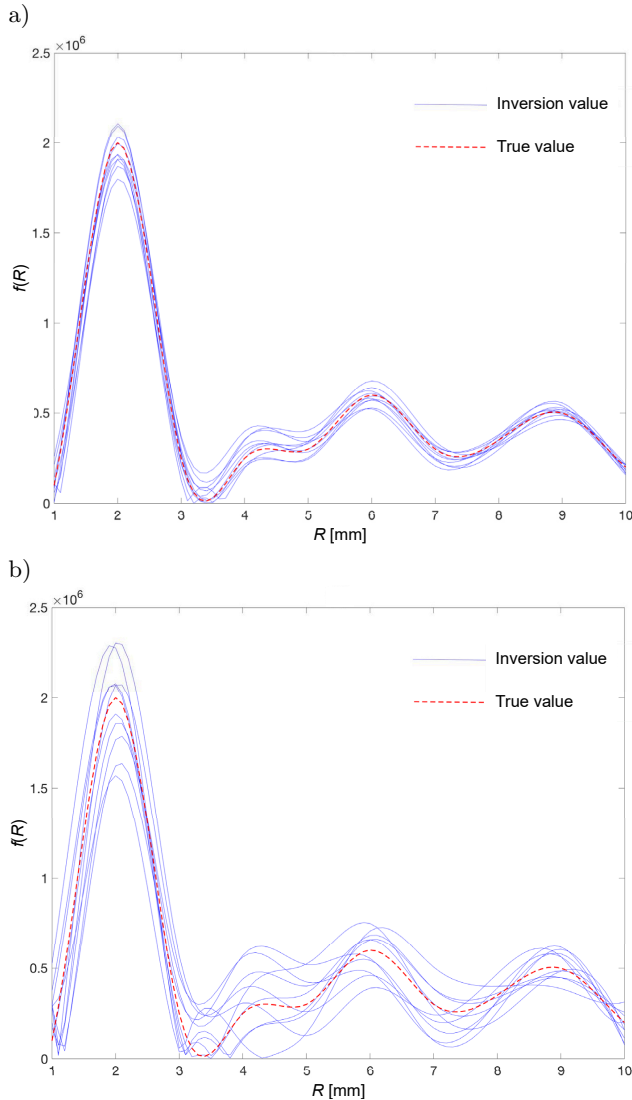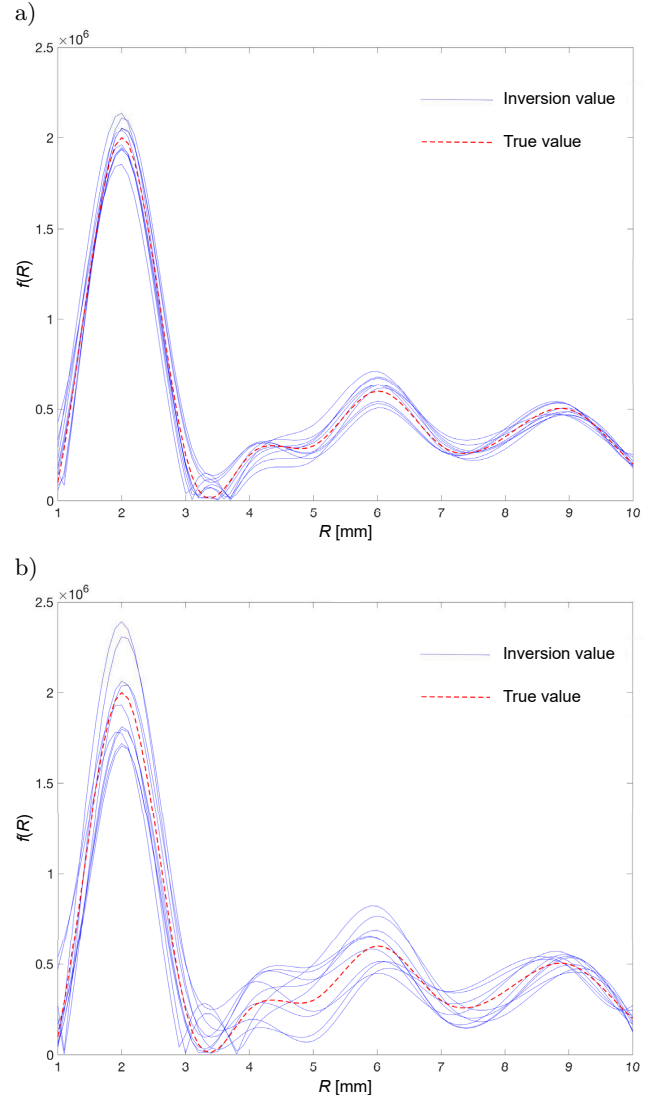
a)

b)

Fig. 4. Inversion results of bubble size distribution for attenuation coefficients error range of: a) 5×10^{-4}; b) 1×10^{-3}.

tained with an attenuation coefficient error range of 5×10^{-4}, whereas a larger local error in bubble size distribution arises with an error range of 1×10^{-3}.

This analysis indicates that sound speed data exhibits a stronger resistance to interference compared to the attenuation data; therefore, the inversion of bubble size distribution is more sensitive to variations in attenuation data. Furthermore, when comparing the results in Fig. 5, it is evident that inaccuracies in attenuation data significantly influence the overall accuracy of the inversion of bubble size distribution when random errors are present in both sound speed and attenuation data. This is further corroborated by the objective function $E(f)$ in Eq. (18), where sound speed c_p appears in the denominator and the attenuation coefficient in the numerator. Consequently, the effect of the attenuation coefficient $\alpha^{(m)}$ on the objective function is more pronounced under the same perturbation range of sound speed.
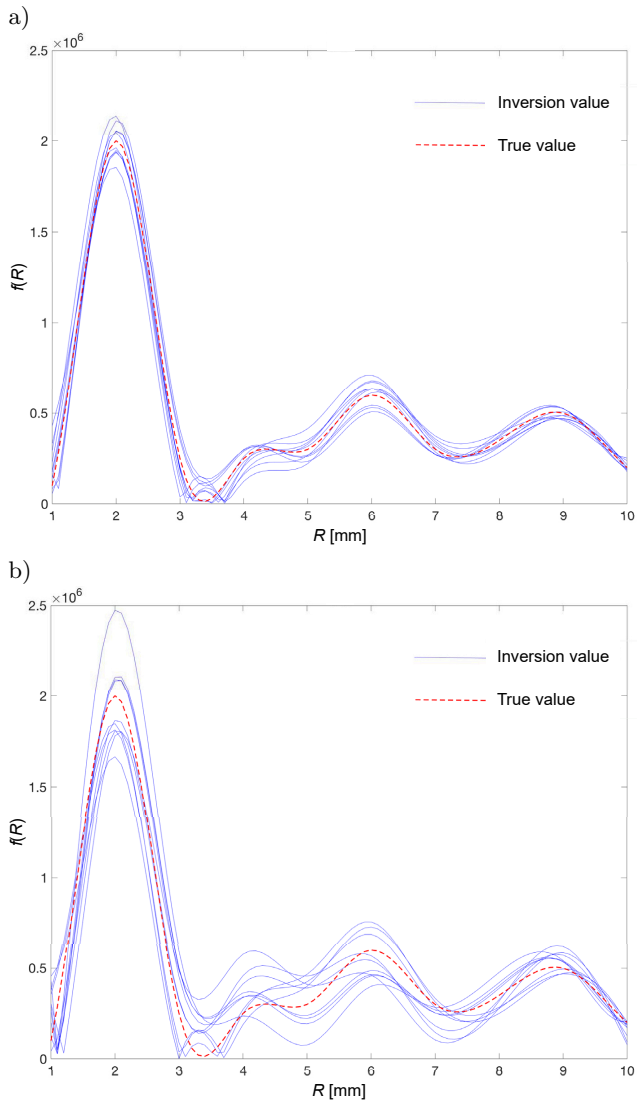
a)

b)

Fig. 3. Inversion results of bubble size distribution for sound speed error range of: a) 1×10^{-3}; b) 2×10^{-3}.

a)

b)

Fig. 5. Inversion results of bubble size distribution for data error range of: a) 5×10^{-4}; b) 1×10^{-3}.

3. Experiments and verification

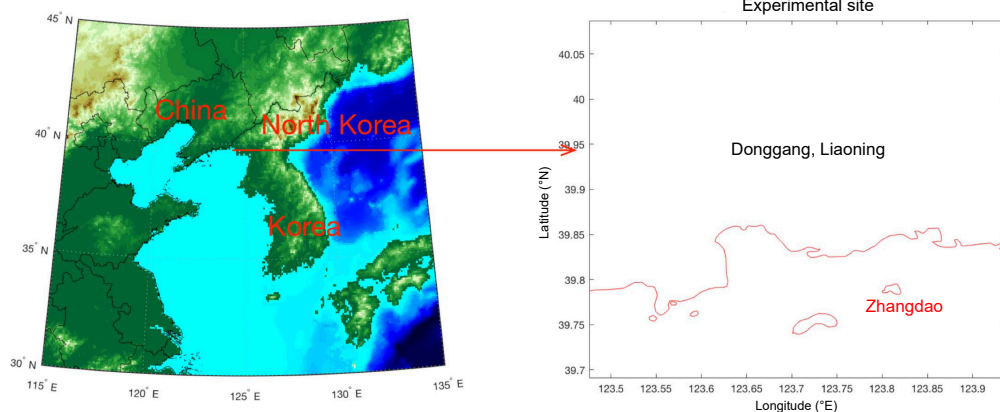In this section, we present an analysis of the experimental results obtained by inverting the bubble size distribution using the method developed in this article. The experimental site is located on the beach of a small island in the Yellow Sea, southwest of Beijingzi Town, Donggang City, Liaoning Province (N39°47′17.36″, E123°49′0.52″), as illustrated in Fig. 6. We selected an intertidal silt zone with a water depth of 3 m–4 m at high tide and a beach that emerges at low tide for the in situ acoustic experiment, due to substantial evidence indicating the presence of shallow gas.

The layout of the in-situ measurement experimental setup is depicted in Fig. 7. Two B&K8103 hydrophones (designated as H1 and H2) are positioned within the sediments at the same horizontal alignment, with a depth difference of 10 cm. These hydrophones are utilized to monitor the acoustic velocity and attenuation of gas-bearing sediments. To preserve the original structure of the sediment, we excavated 50 cm downward next to the designated burial location of the hydrophones and subsequently inserted the devices laterally into their predetermined positions.
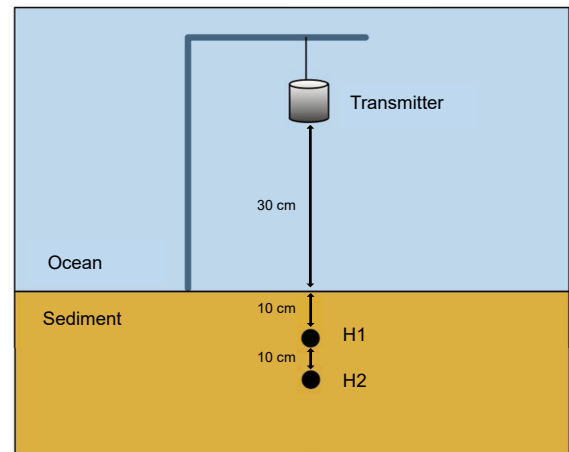

Fig. 7. Diagram of the experimental equipment layout.

The transmitter employed in the experiment is a cylindrical piezoelectric transducer, which operates within a frequency band ranging from 50 Hz to 20 kHz. It is suspended directly above the buried hydrophones

Fig. 6. Experimental site.

using an inverted L-shaped bracket, positioned 30 cm above the sediment surface, with the acoustic axis oriented vertically downward. The transmitted chirp signal spans a frequency range of 100 Hz to 15 kHz and utilizes Blackman window modulation, with a modulated pulse width of 8 ms and a pulse emitted every 1 s. The A/D sampling rate is set at 100 kHz, and the transmission data is recorded every 5 min for a duration of 200 min. Additionally, tidal height is monitored using a miniSVP.

Figure 8 illustrates the time series and frequency spectra recorded by H1 and H2 at two different tidal heights during the experiment. In Figs. 8a and 8b, the time series and frequency spectra captured by H1 and H2 at 21:00, when the water depth was 2.85 m, are presented. Conversely, Figs. 8c and 8d show the corresponding data recorded at 22:15, at a water depth of 3.41 m. Notably, the received signals vary significantly based on the tidal height and the depth of

the hydrophones. The acoustic signals at H1 and H2 can be distinctly identified, as the propagation path length of the acoustic signals received by H2 in the gas-bearing sediment is longer than that received by H1. Consequently, the signal attenuation recorded by H2 is greater than that of H1, leading to a lower amplitude for the H2 signal compared to H1.

The sound speed of gas-bearing sediments at each frequency point can be determined by analyzing the phase difference $\Delta\phi(f)$ between the signals received by the two hydrophones when the transmitted signals have a specified bandwidth. Additionally, the attenuation coefficient can be derived through a comparison of the power spectra of the signals captured by both hydrophones. The sound speed and attenuation coefficients are calculated as follows (Yu *et al.*, 2015):

$$c_p(f) = c\left(1 + \frac{c\Delta\phi(f)}{\omega\delta x}\right), \qquad (24)$$
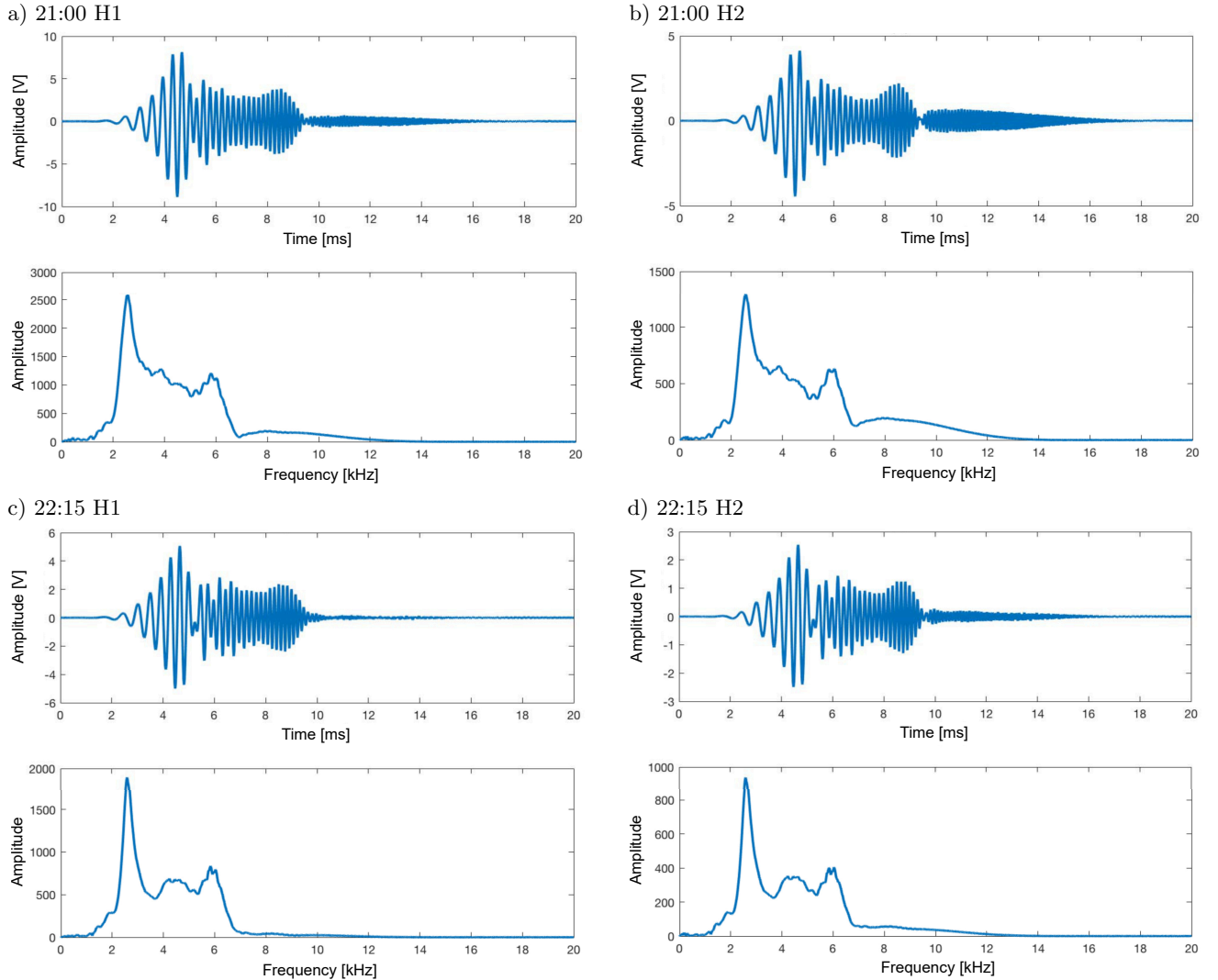

a) 21:00 H1

b) 21:00 H2

c) 22:15 H1

d) 22:15 H2

Fig. 8. Time series and frequency spectra recorded by hydrophones H1 and H2 for two different tidal heights during the experiment.

$$\alpha(f) = 10\frac{1}{\delta x}\lg\left(\frac{A_1(f)}{A_2(f)}\right), \qquad (25)$$

where δx is the distance between H1 and H2 (equal to 10 cm), and $A_1(f)$ and $A_2(f)$ are the power spectral density functions of the signals received by H1 and H2, respectively.

The analysis of sound speed and attenuation was conducted using a wide-band measurement method. Detailed derivations and implementation steps for this approach are provided in Appendix, which supports the experimental findings.

Figure 9 illustrates the relationship between sound speed and attenuation as a function of frequency (100 Hz–6000 Hz) over a half tidal cycle, with the solid line indicating water depth. The water depth varies from 0.65 m at 19:30 to 3.41 m at 22:15, before decreasing to 3.33 m at 22:45. In the upper graph of Fig. 9b, three prominent lines represent the three identified attenuation peaks. Notably, the attenuation

peak within the 4 kHz–6 kHz frequency band exhibits a slight shift towards higher frequencies, which can be attributed to the increase in tidal height and hydrostatic pressure in the sediments. However, no significant frequency shifts are observed for the other two attenuation peaks, likely due to minimal changes in hydrostatic pressure.

To better visualize the frequency shifts associated with hydrostatic pressure variations, the measured changes in sound speed and attenuation coefficient as a function of frequency at both initial and final times are presented in Figs. 9c and 9d. The resonance peaks labeled A–C in Fig. 9d correspond to the three bright lines in Fig. 9b. The frequency of the attenuation peak represented by the dotted line exceeds that of the peak indicated by the solid line, as evidenced by a comparison of the two attenuation curves. The attenuation peaks and their associated frequencies are detailed in Table 3, which also lists the approximate bubble radii for the peak frequencies. According to the frequency

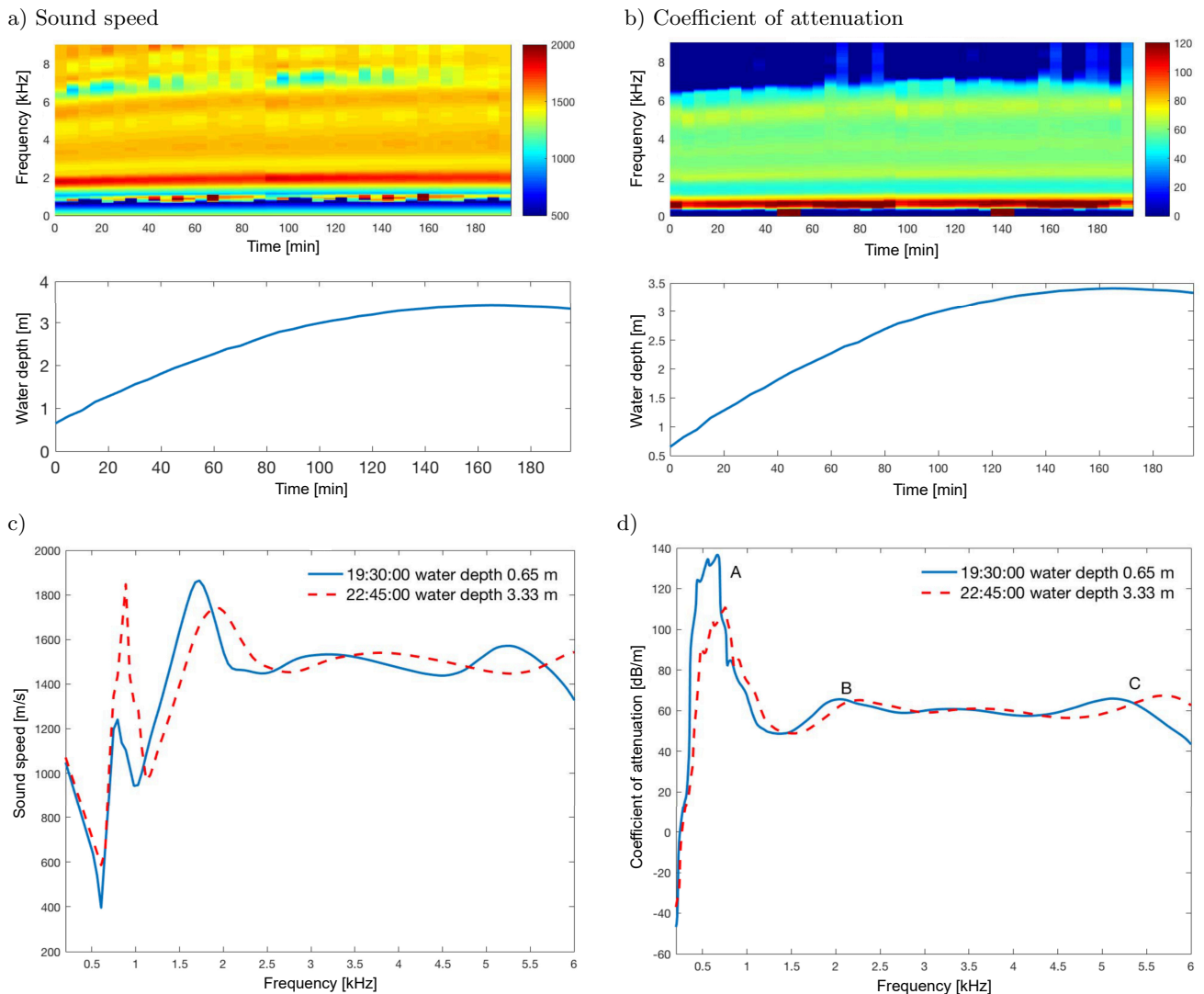a) Sound speed

b) Coefficient of attenuation

c)

d)

Fig. 9. Experimental results: frequency-dependent changes in the speed of sound and damping factor during changes in the height of the water column.

Table 3. Parameters of the attenuation peaks.

Attenuation peaks	19:30:00 Water depth 0.65 m		22:45:00 Water depth 3.33 m		Model predictions
	Resonance peak [Hz]	Attenuation coefficient [dB/m]	Resonance frequency [Hz]	Attenuation coefficient [dB/m]	Bubble radius [mm]
A	664	138	750	110	4.528
B	1853	69	2127	66	1.693
C	4923	68	5626	68	0.575

data in Table 3, the frequency shifts for peaks A, B, and C are 86 Hz, 274 Hz, and 703 Hz, respectively. This observation suggests that smaller bubbles result in larger frequency shifts due to increased hydrostatic pressure. Furthermore, the sound speed represented in Figs. 9a and 9c displays greater complexity, with variations that are more pronounced than the corresponding attenuation data. These fluctuations in sound speed can be attributed to changes in bubble behavior from inductive to capacitive near the bubble resonance frequency, leading to a phase jump at resonance and resulting in significant fluctuations in sound speed.

The frequency of attenuation peaks illustrated in Fig. 9 increases with water depth, confirming that the increase in hydrostatic pressure alters the resonance frequency of the bubble. According to Eq. (8), the resonance frequency of the bubble is proportional to the square root of hydrostatic pressure and inversely proportional to the bubble radius. This relationship suggests that smaller bubble radii will result in larger frequency shifts due to changes in hydrostatic pressure, an observation that aligns with the experimental data. However, the frequency shifts predicted by the model (78 Hz, 232 Hz, and 585 Hz) differ significantly from the measured data (86 Hz, 274 Hz, and 703 Hz). This discrepancy can be attributed to the fact that the measured sound speed and attenuation depend on a specific distribution of bubble sizes, making it inappropriate to interpret frequency shifts for bubbles of varying sizes.

Although the bubble radii correspond to peaks A–C (Table 3), bubble sizes are distributed across marine sediments. The bubble size distribution is derived from sound speed and attenuation data using the proposed inversion method, and the physical parameters of the measured sediment are detailed in Table 4. The best-fit bubble size distribution (ranging from 0.2 mm to 8 mm) is presented in Fig. 10c, with the highest gas content falling within the 6 mm–8 mm range. This range corresponds to the peak of the attenuation coefficient near the 500 Hz frequency and coincides with a sharp fluctuation in sound speed. The fitted sound speed models and attenuation curves are depicted in Figs. 10a and 10b, showing that the magnitudes of these sound speeds and attenuation coefficients

Table 4. Physical parameters of the measured sediment.

	Parameters	Values
Sediment parameters	Grain density	2478 kg/m^3
	Grain diameter	0.145 mm
	Fluid bulk modulus	2.193 Pa × 10^9 Pa
	Grain bulk modulus	3.6 Pa × 10^{10} Pa
	Fluid viscosity	1.002 Pa·s × 10^{-3} Pa·s
	Porosity	0.45
	Fluid density	998.2 kg/m^3
	Structure factor	1.35
Gas parameters	Gas density	1.1691 kg/m^3
	Gas velocity	340 m/s
	Equilibrium pressure	1.01 Pa × 10^5 Pa
	Thermal diffusivity	2.4 m^2/s × 10^{-5} m^2/s
	Surface tension	72.75 N/m × 10^3 N/m
	Ratio of specific heat	1.4

are consistent with the measured attenuation data, thereby validating the proposed inversion method.

4. Conclusion

This study presented an inversion method for estimating bubble size distribution in gas-bearing sediments. The methodology integrates a corrected effective density fluid model with a cubic B-spline approach. The nonlinear inverse problem can be transformed by solving a set of equations involving the coefficients of cubic B-splines. Notably, this method allows for simultaneous estimation of bubble size distribution from measured sound speed and attenuation data. To validate the accuracy and robustness of this method, comparisons with other techniques for measuring bubble size distribution are necessary.

The method proposed in this paper integrates a suitable acoustic model – specifically, an effective density fluid model (ZHENG et al., 2017), adapted to account for gas bubble pulsations – with B-spline expansions. This approach allows for the simultaneous consideration of sound speed and attenuation in addressing the inverse problem. Additionally, the proposed method offers greater applicability for real-time monitoring of shallow gas in marine sediments, compared to conventional inversion methods for bubble size distribution.
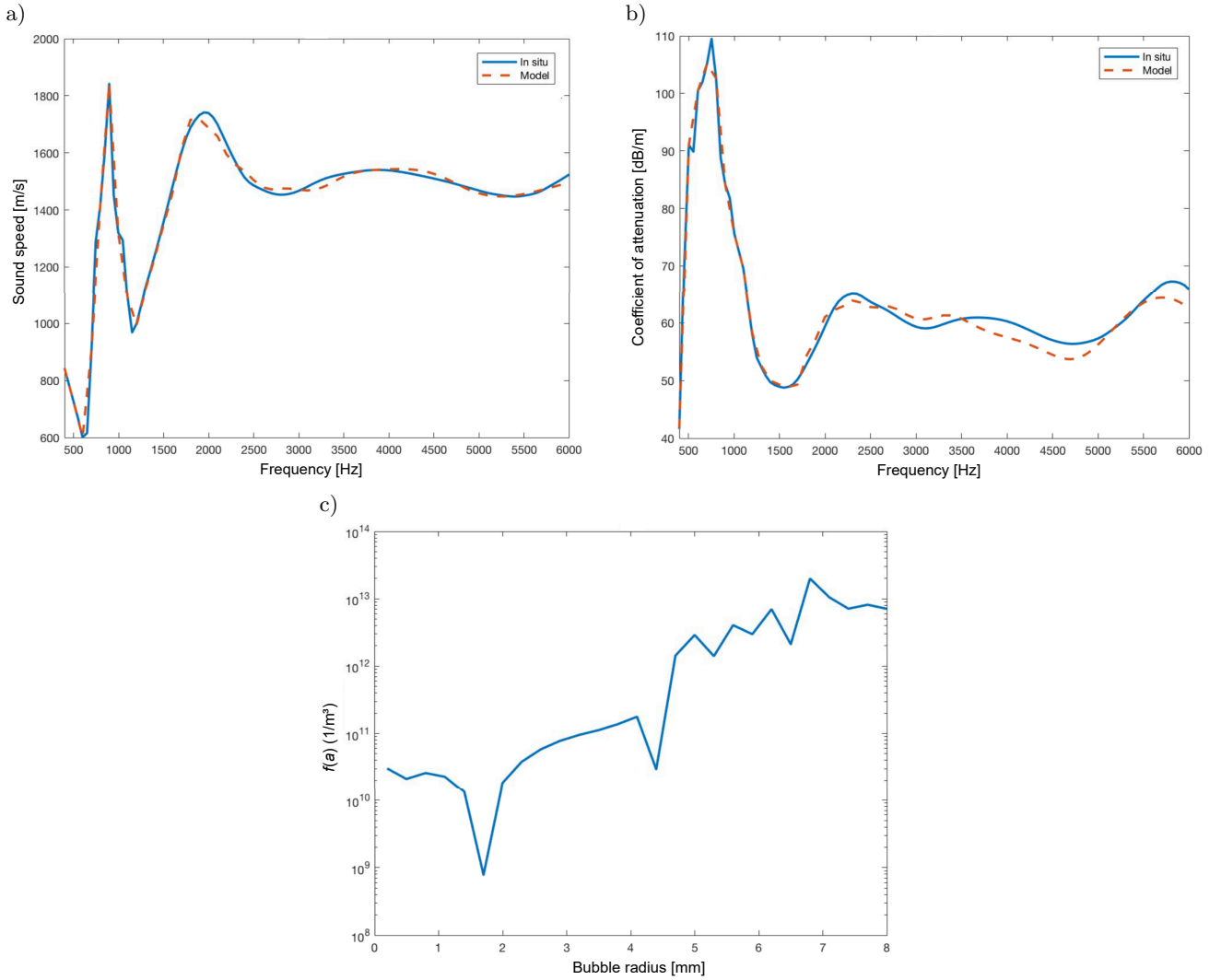
a)

b)

c)

Fig. 10. Model fitting results: a) comparison of measured sound speed with model predictions; b) comparison of measured attenuation coefficient with model predictions; c) inversion results of bubble size distribution.

Appendix

In this appendix, we describe the wide-band method used for measuring sound speed and attenuation in marine sediments. This technique involves the use of a chirp signal modulated by a Blackman window to achieve accurate broadband measurements. The Blackman window offers several advantages, which are:

1) the compressed signal envelope is nearly free of sidelobes, unlike the normal signal, which retains smaller sidelobes. Ignoring these sidelobes can result in the loss of some information;

2) the signal's bandwidth is narrower, reducing distortion from the transmitter transducer, which has a limited bandwidth;

3) the reduced direct waveform shows less significant distortion at the band edges compared to the original signal. For these reasons, the Blackman window is used to modulate the amplitude of the transmit signal. As long as the signal's bandwidth is wide enough and it has high time-delay resolution, the compressed signal can be separated in the time domain, minimizing amplitude and phase distortion. This ensures accurate broadband measurements of sound speed and attenuation.

When a sound wave passes through a sample with thickness $d_1 = x_2 - x_1$, let $p(x_1, \omega)$ be the sound pressure at x_1. In the frequency domain, ignoring the time factor $e^{-j\omega t}$ and assuming a plane wave, the sound pressure received at x_2 can be written as

$$
\begin{aligned}
p(x_2, \omega) &= D_1 p(x_1, \omega) e^{jk(\omega)d_1} \\
&= D_1 p(x_1, \omega) e^{j[\beta(\omega) + j\alpha(\omega)]d_1} \\
&= D_1 p(x_1, \omega) e^{-\alpha(\omega)d_1} \exp\left(j\beta(\omega)d_1\right),
\end{aligned}
\tag{26}
$$

where $k(\omega)$ is the complex wavenumber in the sample; its real part $\beta(\omega) = \omega/c_p(\omega)$ represents the phase velocity, whereas the imaginary part $\alpha(\omega)$ represents the

attenuation coefficient in [Np/m]; $c_p(\omega)$ is the compression wave phase velocity, and D_1 is the transmission coefficient at the water-sediment interface. If this sample with thickness d_1 is considered as a system, its transmission function can be expressed as

$$H_{s1}(j\omega) = D_1 e^{-\alpha(\omega)d_1} \exp\left(j\beta(\omega)d_1\right). \quad (27)$$

Assuming that the distance between the sound source and hydrophone is l and that the sound velocity dispersion and attenuation in the water column are neglected, the transfer function in the water column c_ω can be written as

$$H_{\omega1}(j\omega) = \exp\left(j\omega(l - d_1)/c_\omega\right). \quad (28)$$

Replacing the sample with a thickness of $d_2 (d_2 > d_1)$ and keeping the same source-to-hydrophone distance, we have

$$\begin{aligned} H_{s2}(j\omega) &= D_2 e^{-\alpha(\omega)d_2} \exp\left(j\beta(\omega)d_2\right), \\ H_{\omega2}(j\omega) &= \exp\left(j\omega(l - d_2)/c_\omega\right). \end{aligned} \quad (29)$$

The ratio of the received signal spectrum is as follows:

$$\begin{aligned} H_r(j\omega) &= \left[H_{\omega2}(j\omega)H_{s2}(j\omega)\right] / \left[H_{\omega1}(j\omega)H_{s1}(j\omega)\right] \\ &= \frac{D_2}{D_1} e^{-\alpha(\omega)\Delta d} \exp\{j\left[\beta(\omega)\Delta d - \omega\Delta d/c_\omega\right]\}, \quad (30) \end{aligned}$$

where $\Delta d = d_2 - d_1$. Given $\Delta\phi = \beta(\omega)\Delta d - \omega\Delta d/c_\omega$, the sound speed and attenuation coefficient in the sample can be calculated as follows:

$$c_p = c_\omega \left(1 + \frac{c_\omega \Delta\phi}{\omega \Delta d}\right)^{-1}, \quad (31)$$

$$\alpha_p = -\frac{20 \lg e}{\Delta d} \ln\left[\frac{D_1}{D_2} |H_r(j\omega)|\right], \quad (32)$$

where α_p is the attenuation coefficient in [dB/m]. Thus, the sound speed is determined from the phase difference of the received signal, and the attenuation coefficient is calculated from the ratio of the amplitude spectra of the received signal.

Acknowledgments

References

1. ANDERSON A.L., ABEGG F., HAWKINS J.A., DUNCAN M.E., LYONS A.P. (1998), Bubble populations and acoustic interaction with the gassy floor of Eckernförde Bay, *Continental Shelf Research*, **18**(14–15): 1807–1838, https://doi.org/10.1016/S0278-4343(98)00059-4.

2. ANDERSON A.L., HAMPTON L.D. (1980a), Acoustics of gas bearing sediments. I. Background, *The Journal of the Acoustical Society of America*, **67**(6): 1865–1889, https://doi.org/10.1121/1.384453.

3. ANDERSON A.L., HAMPTON L.D. (1980b), Acoustics of gas bearing sediments. II. Measurements and models, *The Journal of the Acoustical Society of America*, **67**(6): 1890–1903, https://doi.org/10.1121/1.384454.

4. BEST A.I., TUFFIN M.D.J., DIX J.K., BULL J.M. (2004), Tidal height and frequency dependence of acoustic velocity and attenuation in shallow gassy marine sediments, *Journal of Geophysical Research: Solid Earth*, **109**(B8): 589–600, https://doi.org/10.1029/2003JB002748.

5. CHEN J. *et al.* (2023), Elastic wave velocity of marine sediments with free gas: Insights from CT-acoustic observation and theoretical analysis, *Marine and Petroleum Geology*, **150**: 106169, https://doi.org/10.1016/j.marpetgeo.2023.106169.

6. COMMANDER K.W., McDONALD R.J. (1991), Finite-element solution of the inverse problem in bubble swarm acoustics, *The Journal of the Acoustical Society of America*, **89**(2): 592–597, https://doi.org/10.1121/1.400671.

7. DOGAN H., WHITE P. R., LEIGHTON T.G. (2015), Acoustic inversion for gas bubble distributions in marine sediments: Mercury results, *Seabed and Sediment Acoustics*, https://doi.org/10.25144/16045.

8. EDRINGTON T.S., CALLOWAY T.M. (1984), Sound speed and attenuation measurements in gassy sediments in the Gulf of Mexico, *Geophysics*, **49**(3): 297–299, https://doi.org/10.1190/1.1441662.

9. FLEISCHER P., ORSI T., RICHARDSON M., ANDERSON A. (2001), Distribution of free gas in marine sediments: A global overview, *Geo-Marine Letters*, **21**: 103–122, https://doi.org/10.1007/s003670100072.

10. FONSECA L., MAYER L., ORANGE D., DRISCOLL N. (2002), The high-frequency backscattering angular response of gassy sediments: Model/data comparison from the Eel River Margin, California, *The Journal of the Acoustical Society of America*, **111**(6): 2621–2631, https://doi.org/10.1121/1.1471911.

11. KARPOV S.V., KLUSEK Z., MATVEEV A.L., POTAPOV A.I., SUTIN A.M. (1996), Nonlinear interaction of acoustic waves in gas-saturated marine sediments, *Acoustical Physics*, **42**(4): 464–470.

12. LEIGHTON T.G. (2007), Theory for acoustic propagation in marine sediment containing gas bubbles which may pulsate in a non-stationary nonlinear manner, *Geophysics Research Letters*, **34**(17): 607, https://doi.org/10.1029/2007GL030803.

13. LEIGHTON T.G., ROBB G.B.N. (2008), Preliminary mapping of void fractions and sound speeds in gassy

marine sediments from subbottom profiles, *The Journal of the Acoustical Society of America*, **124**(5): EL313–EL320, https://doi.org/10.1121/1.2993744.

14. MANTOUKA A., DOGAN H., WHITE P.R., LEIGHTON T.G. (2016), Modelling acoustic scattering, sound speed, and attenuation in gassy soft marine sediments, *The Journal of the Acoustical Society of America*, **140**(1): 276–282, https://doi.org/10.1121/1.4954753.

15. RICHARDSON M.D., DAVIS A.M. (1998), Modeling methane-rich sediments of Eckernförde Bay, *Continental Shelf Research*, **18**(14–15): 1671–1688, https://doi.org/10.1016/S0278-4343(98)00074-0.

16. SHANKAR U., SINHA B., THAKUR N.K., KHANNa R. (2005), Amplitude-versus-offset modeling of the bottom simulating reflection associated with submarine gas hydrates, *Marine Geophysical Research*, **26**(1): 29–35, https://doi.org/10.1007/s11001-005-2134-1.

17. SHANKAR U., THAKUR N.K., ASHALATHA B. (2006), Fluid flow related features as an indicator of potential gas hydrate zone: Western continental margin of India, *Marine Geophysical Research*, **27**(3): 217–224, https://doi.org/10.1007/s11001-006-9001-6.

18. YU S., HUANG Y., LIU B., WANG F., ZHENG G. (2015), A wide-band method for sound speed and attenuation measurement in sediments, *Acta Acustica*, **40**(5): 682–694, https://doi.org/10.15949/j.cnki.0371-0025.2015.05.009.

19. TÓTH Z., SPIESS V., KEIL H. (2015), Frequency-dependence in seismo-acoustic imaging of shallow free gas due to gas bubble resonance, *Journal of Geophysical Research-Solid Earth*, **120**(12): 8056–8072, https://doi.org/10.1002/2015JB012523.

20. WILKENS R.H., RICHARDSON M.D. (1998), The influence of gas bubbles on sediment acoustic properties: In situ, laboratory, and theoretical results from Eckernförde Bay, Baltic sea, *Continental Shelf Research*, **18**(14): 1859–1892, https://doi.org/10.1016/S0278-4343(98)00061-2.

21. YARINA M., KATSNELSON B., GODIN O.A. (2023), Modal structure of the sound field in a shallow-water waveguide with a gassy sediment layer: Experiment and theory, *The Journal of the Acoustical Society of America*, **153**(3): A375–A375, https://doi.org/10.1121/10.0019231.

22. ZHANG D., YANG J., WANG H., LI X. (2023), Prediction model of strength properties of marine gas-bearing sediments based on compressional wave velocity, *Applied Ocean Research*, **135**: 103562, https://doi.org/10.1016/j.apor.2023.103562.

23. ZHENG G.Y., HUANG Y.W. (2016), Effect of linear bubble vibration on wave propagation in unsaturated porous medium containing air bubbles, *Acta Physica Sinica*, **65**(23): 234301, https://doi.org/10.7498/aps.65.234301.

24. ZHENG G.Y., HUANG Y. W., HUA J., XU X., WANG F. (2017), A corrected effective density fluid model for gassy sediments, *The Journal of the Acoustical Society of America*, **141**(1): EL32–EL37, https://doi.org/10.1121/1.4973616.